Three-dimensional acoustic Chern insulators with arbitrary Chern vectors

Linyun Yang,[1,2,*] Xiang Xi,[1,3,*] Yan Meng,[1,3,*] Zhenxiao Zhu,[1,*] Ying Wu,[4] Jingming Chen,[1] Minqi Cheng,[1] Kexin Xiang,[1] Perry Ping Shum,[1] Yihao Yang,[5] Hongsheng Chen,[5] Jian Li,[6] Bei Yan,[1,7,†] Gui-Geng Liu,[8,‡] Baile Zhang,[9,10,§] and Zhen Gao[1,‖]

[1]*State Key Laboratory of Optical Fiber and Cable Manufacturing Technology, Department of Electronic and Electrical Engineering, Guangdong Key Laboratory of Integrated Optoelectronics Intellisense, Southern University of Science and Technology, Shenzhen 518055, China*

[2]*College of Aerospace Engineering, Chongqing University, Chongqing 400030, China*

[3]*School of Electrical Engineering and Intelligentization, Dongguan University of Technology, Dongguan 523808, China*

[4]*School of Science, Nanjing University of Science and Technology, Nanjing 210094, China*

[5]*Interdisciplinary Center for Quantum Information, State Key Laboratory of Modern Optical Instrumentation, ZJU-Hangzhou Global Science and Technology Innovation Center, College of Information Science and Electronic Engineering, ZJU-UIUC Institute, Zhejiang University, 310027 Hangzhou, China*

[6]*School of Science, Westlake University, 18 Shilongshan Road, Hangzhou 310024, Zhejiang Province, China*

[7]*Hubei Province Key Laboratory of Systems Science in Metallurgical Process, and College of Science, Wuhan University of Science and Technology, Wuhan 430081, China*

[8]*Department of Electronic and Information Engineering, School of Engineering, Westlake University, Hangzhou 310030, China*

[9]*Division of Physics and Applied Physics, School of Physical and Mathematical Sciences, Nanyang Technological University, Singapore 637371, Singapore*

[10]*Centre for Disruptive Photonic Technologies, The Photonics Institute, Nanyang Technological University, Singapore 639798, Singapore*

(Received 26 October 2023; accepted 23 May 2025; published 18 June 2025)

The Chern vector is a vectorial generalization of the scalar Chern number, being able to characterize the topological phases of three-dimensional (3D) Chern insulators. Such a vectorial generalization extends the applicability of Chern-type bulk-boundary correspondence from one-dimensional edge states to two-dimensional surface states, whose unique features, such as robust chiral surface states and forming nontrivial torus knots or links in the surface Brillouin zone, have been demonstrated recently in 3D photonic crystals. However, to date, the Chern vectors have been limited to the simplest form with only one nonzero component, resulting in the chiral surface states only propagating along four side surfaces parallel to the Chern vector, and the surface-state torus knots or links emerging, not on the surface of a single crystal as in other 3D topological phases, but only along an internal domain wall between two crystals with perpendicular Chern vectors. Here, we extend the 3D Chern insulator phase to acoustic crystals for sound waves and propose a scheme to construct an arbitrary Chern vector with multiple nonzero components that allow the chiral surface states to propagate along all six surfaces and the emergence of surface-state torus knots or links on the surface of a single crystal. These results provide a complete picture of bulk-boundary correspondence for Chern vectors and may have potential applications in designing topological acoustic devices.

DOI: 10.1103/qthq-fbt1

I. INTRODUCTION

The topological invariant of Chern number, which is used to characterize two-dimensional (2D) Chern insulators with chiral edge states [1–11], as depicted in Fig. 1(a), has been generalized from an integer scalar $c \in \mathbb{Z}$ to a vector [12,13] in the form of $\boldsymbol{C} = (c_1,\ c_2, c_3)$ that can characterize three-dimensional (3D) Chern insulators with chiral surface states. A remarkable feature of the bulk-boundary correspondence arising from the vectorial nature of the Chern vector is that topological surface states of 3D Chern insulators can form nontrivial torus knots or links in the surface Brillouin zone, as recently demonstrated in 3D photonic crystals [14–16]. However, up to now, the topological Chern vectors have been limited to the simplest form, $\boldsymbol{C} = (0,\ 0, c_3)$ with a single nonzero component, restricting the chiral surface states to reside only on four side surfaces that are parallel to the Chern vector and the Fermi loop wraps around the surface Brillouin zone along only one direction, as shown in Fig. 1(b).

*These authors contributed equally to this work.
†Contact author: yanbei@wust.edu.cn
‡Contact author: liuguigeng@westlake.edu.cn
§Contact author: blzhang@ntu.edu.sg
‖Contact author: gaoz@sustech.edu.cn

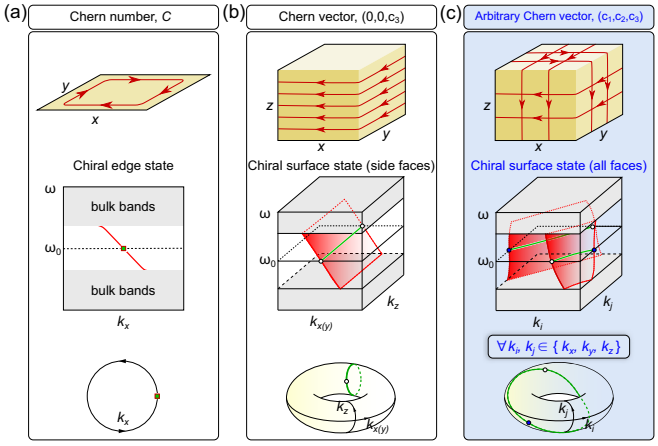

FIG. 1. Schematics of the topological properties of the chiral edge (surface) states in 2D (3D) Chern insulators with different topological invariants. (a) 2D Chern insulators characterized by a nonzero Chern number C and chiral edge states. (b) 3D Chern insulators characterized by a single-nonzero-component Chern vector $(0,\ 0,\ \boldsymbol{c}_3)$ and chiral surface states on four side surfaces. (c) 3D Chern insulators characterized by an arbitrary multiple-nonzero-component Chern vector $(\boldsymbol{c}_1, \boldsymbol{c}_2, \boldsymbol{c}_3)$ and chiral surface states on all surfaces.

Consequently, to form nontrivial surface-state torus knots or links that wrap around two directions, one has to construct an internal domain wall between two 3D Chern insulators with perpendicular Chern vectors [14–16]. This is not the complete picture of the bulk-boundary correspondence for the Chern vectors in 3D Chern insulators, since it is still unclear how to achieve an arbitrary Chern vector with multiple nonzero components.

Along a separate line of development, the acoustic analog of Chern insulators, known as acoustic Chern insulators [17–20], has stimulated the rise of research in topological acoustics [21–29], with promising sound manipulation with robust chiral edge states that are immune to backscattering from defects and disorders. However, despite much recent progress, the acoustic Chern insulators have thus far been limited to two dimensions.

In this paper, we extend the concept of Chern vector to acoustic crystals and propose a scheme to construct an acoustic 3D Chern insulator. In particular, the acoustic 3D Chern insulator exhibits an arbitrary Chern vector with multiple nonzero components $\boldsymbol{C} = (c_1, c_2, c_3)$, as shown in Fig. 1(c), allowing the chiral surface states to reside on all surfaces and the emergence of surface-state torus knots or links on the surface of a single 3D Chern insulator. Moreover, we also show the phenomenon of successive topological negative refraction at three adjacent facets of a single crystal, in which acoustic chiral surface states can pass through sharp edges continuously in 3D space through negative refraction without backscattering, being different from previously proposed topological negative refraction [30,31].

This paper is organized as follows. In Sec. II, we introduce two 3D tight-binding models developed from the celebrated Haldane model [1], which we term as stacked and tilted 3D Haldane models, respectively. Our analyses on the bulk band topology, phase diagram, and surface dispersions

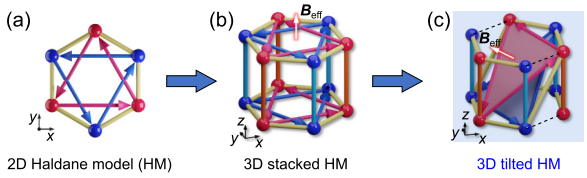

FIG. 2. The design strategy to construct the tight-binding models. (a) 2D Haldane model. (b) 3D Haldane model. (c) 3D tilted Haldane model.

unambiguously show that these two models can exhibit 3D Chern insulating phases with distinct topological Chern vectors $\boldsymbol{C} = (0,\ 0,\ 1)$ and $\boldsymbol{C} = (-1,\ -1,\ 1)$. In Sec. III, we implement the stacked/tilted 3D Haldane models in acoustic crystals by introducing circulating air flows to mimic the nonreciprocal couplings to break the time-reversal symmetry (TRS). Furthermore, we perform first-principles finite element simulations on the acoustic 3D Chern insulators to reveal the topologically protected chiral transport of sound waves on the surfaces of the 3D acoustic Chern insulators. Finally, we summarize the main results and conclude this work in Sec. IV.

II. TIGHT-BINDING MODEL AND THEORY

To construct a 3D Chern insulator (e.g., 3D Haldane model), we first start by periodically stacking 2D Chern insulators (e.g., 2D Haldane model) along the z axis, as depicted in Figs. 2(a) and 2(b). Such a layer-stacking strategy has been employed to realize a photonic 3D Chern insulator [14] with the Chern vector taking the simplest form of $\boldsymbol{C} = (0,\ 0, c_3)$ with only a single nonzero component. Here, we step further and propose a 3D tilted Haldane model, which exhibits a Chern vector $\boldsymbol{C} = (c_1, c_2, c_3)$ with multiple nonzero components, as shown in Fig. 2(c). By realizing the Chern vector with multiple nonzero Chern components, we are enabled to reveal the complete picture of the Chern-type bulk-boundary correspondence, as we will demonstrate below.

A. 3D Chern insulator in a stacked Haldane model

We first consider the 3D stacked Haldane model, i.e., the simplest example of a 3D Chern insulator characterized by a Chern vector $\boldsymbol{C} = (0,\ 0,\ 1)$. As shown in Fig. 3(a), adjacent layers of 2D Haldane models are interconnected by vertical couplings labeled as $t_{a,b}$. Note that the tight-binding configuration in Fig. 3(a) is slightly different from that in Fig. 2(b), where we have added additional chiral couplings t_c (green rods). The chiral couplings t_c provide an extra degree of freedom to tune the bulk dispersions of the 3D stacked Haldane model and do not affect its topological properties. Here we set $t_c = (t_a + t_b)/3$ to guarantee the band degenerate points are always the type-I Weyl points to facilitate opening a complete 3D bulk band gap with a small TRS breaking. The 2D Haldane model in each layer is a honeycomb lattice with nearest-neighbor (NN) and next-nearest-neighbor (NNN) hoppings being t_1 and $t_2 \exp(\pm i\phi)$, respectively. The arrows in Fig. 3(a) indicate the direction along which the complex hoppings accumulate a phase ϕ. The Bloch Hamiltonian of

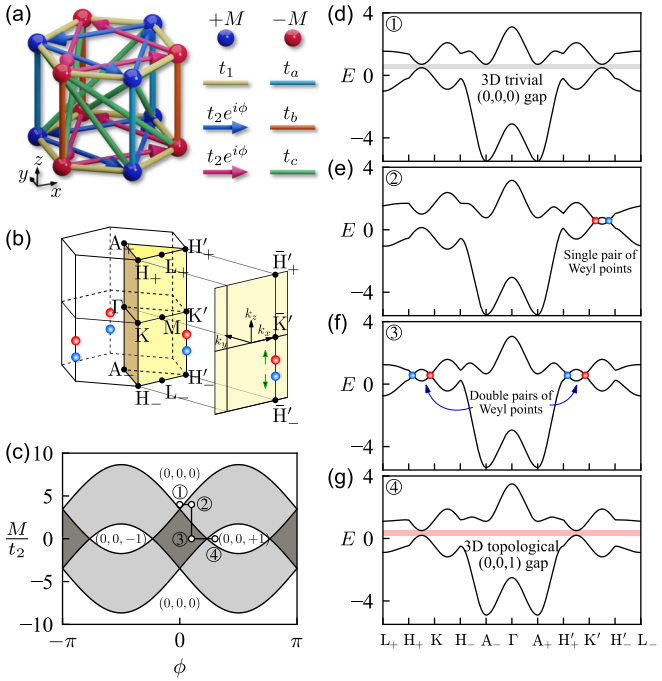

FIG. 3. The 3D stacked Haldane model and its phase diagram and bulk band structures. (a) The tight-binding configuration of the 3D Haldane model. (b) The 3D bulk BZ and the projected $(0\bar{1}0)$ surface BZ, the red and blue spheres represent the type-I Weyl points. (c) Phase diagram of the 3D Haldane model. (d)–(g) Bulk band structures of the 3D Haldane model for phases ①–④ marked in (c), among which ④ represents a 3D Chern insulator with a Chern vector $\boldsymbol{C} = (0,\ 0,\ 1)$.

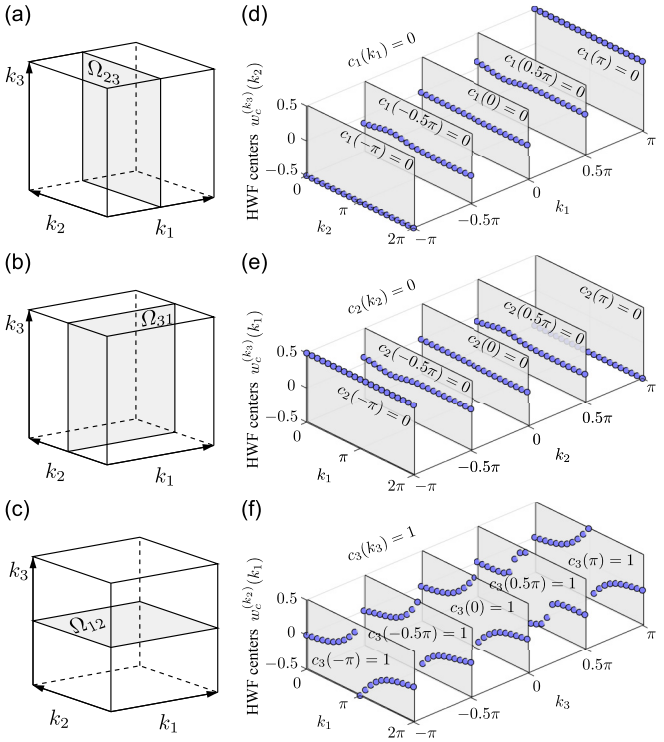

FIG. 4. Calculations of the Chern numbers $C_{\mu\nu}(k_\varepsilon) = (1/2\pi)\iint \Omega_{\mu\nu} dk_\mu dk_\nu$ of phase ④ in different subspace of the 3D BZ based on the Wilson-loop approach. (a)–(c) illustrate the 2D slices of the 3D BZ, and (d)–(f) display the corresponding Wannier center flows at various cross sections.

the 3D stacked Haldane model in momentum space reads

$$H(\boldsymbol{k}) = \begin{bmatrix} \Delta^+ & \Phi^- \\ \Phi^+ & \Delta^- \end{bmatrix} \tag{1}$$

in which $\Delta^\pm = \pm M + 2t_{a,b}\cos k_3 + \Theta^\pm(t_2,\phi) + \Theta^\pm(t_c,k_3)$ and $\Phi^\pm = t_1[1+\exp(\pm ik_1)+\exp(\pm ik_2)]$, with $\Phi^\pm(t,\xi) = 2t[\cos(\xi \pm k_1)+\cos(\xi \mp k_2)+\cos(\xi \mp k_1 \pm k_2)]$. Here $k_i = \boldsymbol{k}\cdot\boldsymbol{a}_i \in [0, 2\pi]$ for $i = 1,\ 2,\ 3$ denotes the reduced wave number, and the primitive lattice vectors are $\boldsymbol{a}_1 = (a,\ 0,\ 0)$, $\boldsymbol{a}_2 = (a/2, \sqrt{3}a/2,\ 0)$ and $\boldsymbol{a}_1 = (0,\ 0,\ h)$, where a and h are the in-plane and out-of-plane lattice constants, respectively.

The Hamiltonian of the 3D stacked Haldane model in Eq. (1) supports rich topological phases such as Weyl semimetals and 3D Chern insulators with different parameterizations of ϕ and M/t_2, i.e., the TRS and the inversion symmetry (IS)-breaking strengths. The phase diagram obtained by tracing the band degenerate points on the $(\phi, M/t_2)$ plane is presented in Fig. 3(c), in which the dark (light) gray regions represent Weyl semimetals with double (single) pairs of Weyl points, and the white regions represent 3D insulating phases, as evidenced by the bulk band structures of the four typical topological phases (labeled as ①–④ in the phase diagram) shown in Figs. 3(d)–3(g). The 3D insulating phases can be further distinguished as 3D trivial insulators and 3D Chern insulators depending on their topological invariants, i.e., the Chern vector defined in the 3D Brillouin zone (BZ), a three-torus T^3 parameterized by $(k_1, k_2, k_3) \in [0,\ 2\pi]^3$. By slicing the T^3 to T^2 on three different orthogonal planes, we can compute three Chern numbers on each T^2 subspace as

$$C_{\mu\nu}(k_\varepsilon) = (1/2\pi)\iint_{T^2} \Omega_{\mu\nu} dk_\mu dk_\nu \tag{2}$$

with $\mu,\ \nu,\ \varepsilon$ being the cyclic indices labeling the three momentum dimensions, $\Omega_{\mu\nu}(\boldsymbol{k}) = \partial_{k_\mu}\boldsymbol{A}_\nu(\boldsymbol{k}) - \partial_{k_\nu}\boldsymbol{A}_\mu(\boldsymbol{k})$ is the Berry curvature, and $\boldsymbol{A}_\mu(\boldsymbol{k}) = \langle \boldsymbol{u}(\boldsymbol{k})|i\nabla_{k_\mu}|\boldsymbol{u}(\boldsymbol{k})\rangle$ is the Berry connection wherein $\boldsymbol{u}(\boldsymbol{k})$ is the cell-periodic part of the Bloch eigenstate of the bulk Hamiltonian at $\boldsymbol{k}$. Therefore, the Chern vector is a triplet of Chern numbers computed on each of the T^2 subspaces, which is denoted as $\boldsymbol{C} = (C_{23}, C_{31}, C_{12})$ or $\boldsymbol{C} = (c_1, c_2, c_3)$ [13]. For the 3D stacked Haldane model in Eq. (1) with tight-binding parameters in phase ①, our Wilson-loop approach-based calculations (Fig. 4) show that the Chern vector is $\boldsymbol{C} = (0, 0, 1)$, indicating that it is a 3D Chern insulator.

The nonzero component $C_{12}(k_3) \equiv 1$ indicates that chiral edge states should exist along the boundaries of any xy cross sections for arbitrary $k_3 \in [0, 2\pi]$, which constructs the chiral surface states on the four side faces of a finite 3D crystal. On the other hand, the other two zero Chern numbers ($C_{23} = C_{31} = 0$) result in the absence of chiral surface states on the top and bottom faces. A full-wave simulation on the transportation of the chiral surface states on a 3D acoustic crystal is carried out in Sec. III to support the prediction. We can sum up that the presence (absence) of chiral surface

states on a particular surface of a 3D crystal is determined by whether the Chern vector has a nonzero (zero) component along the parallel vector of that surface. This principle can be applied not only to the case of $\boldsymbol{C} = (0,\ 0, c_3)$ but also to the case of an arbitrary Chern vector $\boldsymbol{C} = (c_1,\ c_2, c_3)$, as we will demonstrate below.

B. 3D Chern insulator in a tilted 3D Haldane model

The Chern vector $\boldsymbol{C} = (0,\ 0,\ 1)$ of the 3D Chern insulators discussed above has only a single nonzero Chern number $c_3 = 1$. In that case, the chiral surface states are forbidden on the top and bottom surfaces but only exist on the four side surfaces, which can be qualitatively understood as a stacking of the chiral edge states on the boundaries of 2D Chern insulators. However, such an example is not sufficient to demonstrate the vectorial nature of the topological Chern vectors in 3D crystals. In this section, to reveal the unique vectorial nature of the Chern vectors, we propose a tilted 3D Haldane model characterized by a Chern vector whose components are all nonzero.

The tight-binding configuration of a unit cell of the tilted 3D Haldane model is modified from the stacked 3D Haldane model. In the stacked 3D Haldane model, the nonreciprocal couplings $t_2 \exp(\pm i\phi)$ only exist between two sites in the same layer. For the tilted 3D Haldane model, we introduce some NNN nonreciprocal couplings between sites in adjacent layers, as shown in Fig. 5(a). Meanwhile, four NN couplings are replaced by two slanted interlayer couplings between different sublattice sites in adjacent layers. The Hamiltonian of such a tilted 3D Haldane model can be written as

$$\tilde{H}(\boldsymbol{k}) = \begin{bmatrix} \tilde{\Delta}^{+} & \tilde{\Phi}^{-} \\ \tilde{\Phi}^{+} & \tilde{\Delta}^{-} \end{bmatrix}, \tag{3}$$

where $\tilde{\Phi}^{\pm} = t_1[\exp(\mp ik_3) + \exp(\pm ik_1) + \exp(\pm ik_2)]$ and $\tilde{\Delta}^{\pm} = \pm M + 2t_{a,b}\cos k_3 + \tilde{\Theta}^{\pm}(t_2, \phi)$ with $\tilde{\Theta}^{\pm}(t, \xi) = 2t[\cos(\xi \pm k_1 \pm k_3) + \cos(\xi \mp k_2 \mp k_3) + \cos(\xi \mp k_1 \pm k_2)]$. As an example, we set the tight-binding parameters $t_2 = -0.2, t_a = -t_b = 0.2,\ \ t_c = 0,\ \ \text{and}\ \ \phi = \pi/2$. The calculated bulk band structure shows that there is a complete energy gap in the range of $[-0.64,\ 0.64]$ in the 3D BZ, as shown in the left panel of Fig. 5(b), which can be further confirmed by the bulk density-of-states (DOS) shown in the right panel of Fig. 5(b). We then calculate its Chern vector based on the Wilson-loop approach, as shown in the right panels of Figs. 5(c)–5(e), from which we can see that the Chern vector is $\boldsymbol{C} = (-1,\ -1,\ 1)$, with all components being nonzero. This Chern vector guarantees the existence of chiral surface states on all surfaces of a finite 3D crystal, as we will demonstrate in the next section.

III. RESULTS AND DISCUSSION

In the previous section, we have studied the stacked and tilted 3D Haldane model, which exhibits a 3D Chern insulating phase with nontrivial Chern vectors $\boldsymbol{C} = (0,\ 0,\ 1)$ and $\boldsymbol{C} = (-1,\ -1,\ 1)$, respectively. Moreover, we find that the orientation of the Chern vector is closely related to the configuration of the nonreciprocal couplings. In this section, we will demonstrate how to realize these 3D Chern

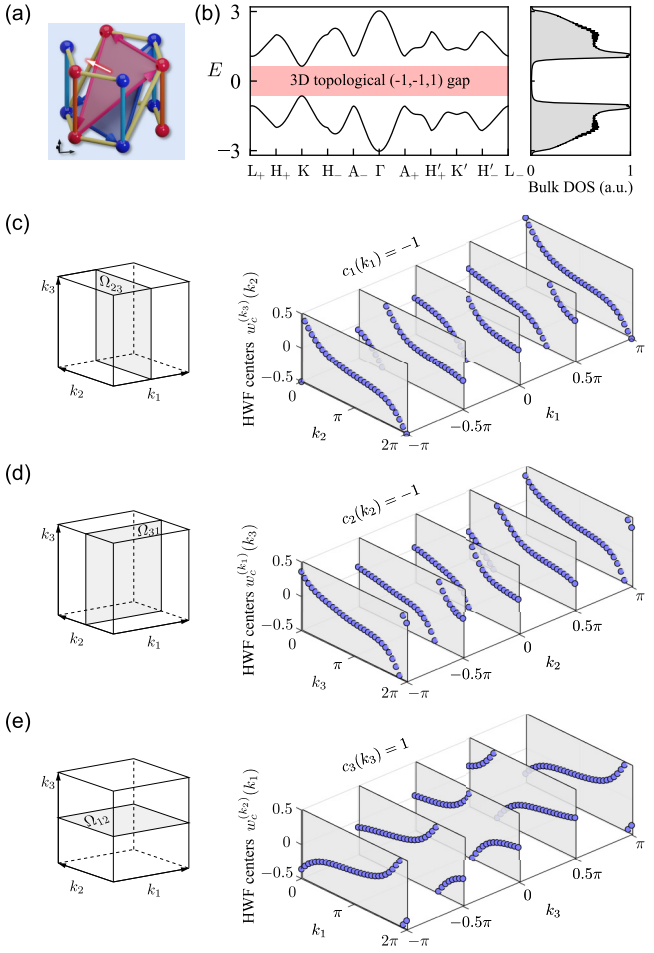

FIG. 5. The tilted 3D Haldane model. (a) The tight-binding configuration of a unit cell of the tilted 3D Haldane model. (b) The bulk band structure (left) and the bulk density-of-states (right). (c)–(e) The 2D slices of the 3D BZ (left) and the corresponding Wannier center flow at various cross sections (right), revealing that the Chern vector is $\boldsymbol{C} = (-1,\ -1,\ 1)$.

insulating phases in acoustic crystals. Furthermore, we will also propose a scheme to achieve an arbitrary Chern vector $\boldsymbol{C} = (-N_1,\ -N_2, N_3)$ by adopting a supercell comprising $N_1 \times N_2 \times N_3$ elementary unit cells of the tilted 3D Haldane model.

Acoustic crystals have been widely adopted as an ideal platform to imitate electronic crystals, with the frequency playing the role of energy. In the acoustic crystal design, acoustic cavities and thin tubes connecting them are treated as artificial atoms and couplings, respectively. In addition, we adopt a circulating air flow to introduce nonreciprocal acoustic couplings to break the TRS. In the presence of a steady-state background circulating air flow, the propagation of acoustic waves obeys the governing equation [17,20]

$$\frac{1}{\rho}\nabla \cdot \rho \nabla \varphi(\boldsymbol{r}, t) - (\partial_t + v \cdot \nabla) \cdot \frac{1}{c_0^2}(\partial_t + v \cdot \nabla)\varphi(\boldsymbol{r}, t) = 0, \tag{4}$$

where $\varphi(\boldsymbol{r}, t)$ is the acoustic particle velocity potential, ρ is the density of air, c_0 is the sound speed, and $\boldsymbol{v}$ is the velocity

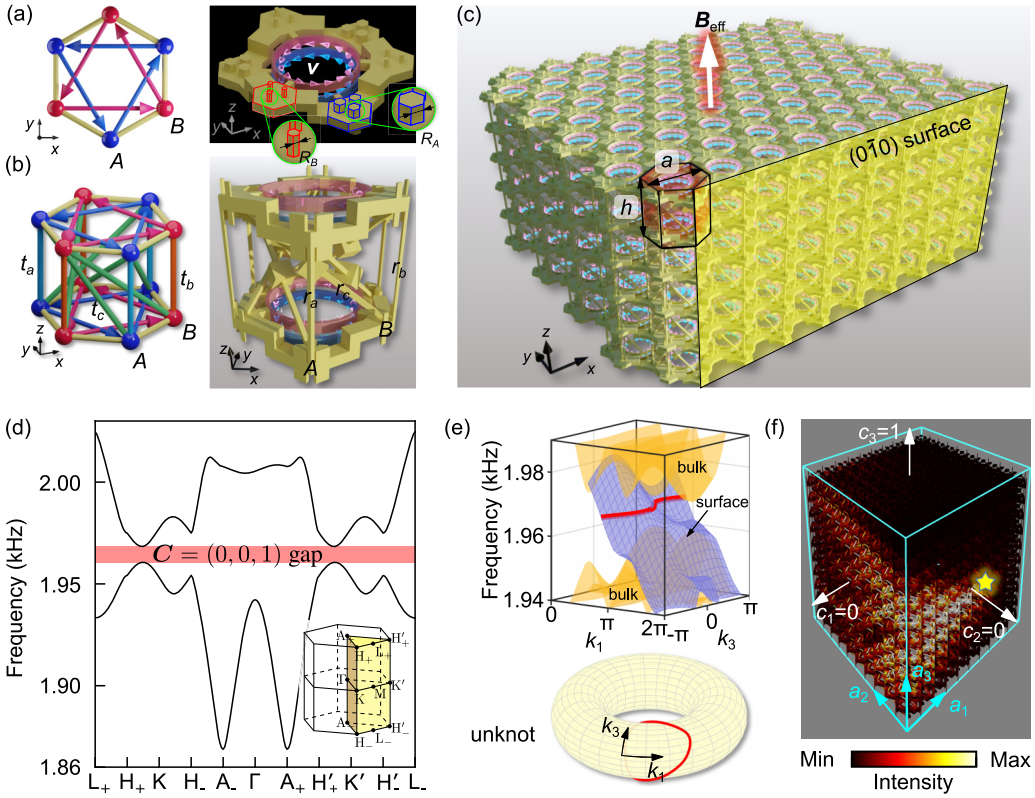

FIG. 6. Acoustic 3D Chern insulator with a Chern vector $\boldsymbol{C} = (0,\ 0,\ 1)$. The tight-binding configuration and the acoustic crystal design of (a) a 2D Haldane model and (b) its 3D generalization. The red and blue arrows in the right panels indicate the circulating airflow among sites in sublattice A and sublattice B, respectively. (c) Acoustic realization of a 3D Haldane model constructed by the unit cell shown in the right panel of (b), which exhibits an effective magnetic field $\boldsymbol{B}_{\rm eff}$ similar to the external magnetic field in previous 3D photonic Chern insulators. (d) The bulk band diagram of the acoustic 3D Chern insulator with a nontrivial topological $\boldsymbol{C} = (0,\ 0,\ 1)$ bandgap. (e) The $(0\bar{1}0)$-surface dispersion of the acoustic 3D Chern insulator and the unknot formed by the Fermi loop. (f) Full-wave simulated acoustic intensity distributions of the chiral surface states exited by a point source (yellow star) at the midgap frequency 1.968 kHz.

of the background circulating flow. When considering $v \ll c_0$ and introducing a new variable $\psi(\boldsymbol{r}) = \sqrt{\rho(\boldsymbol{r})}\varphi(\boldsymbol{r})$, the wave equation can be linearized as

$$(\nabla - i\boldsymbol{A}) \cdot (\nabla - i\boldsymbol{A})\psi + V\psi = 0 \ , \tag{5}$$

where the scalar and vector potentials are $V = \omega^2/c_0^2 - |\nabla \ln\rho|^2/4 - \nabla^2 \ln\rho/2$ and $\boldsymbol{A} = -\omega \boldsymbol{v}/c_0^2$, respectively. In our acoustic crystal design, we utilize the flow velocity (thus also the vector potential) to break the TRS. The numerical calculations of the bulk band structure, chiral surface states, and the acoustic wave transportation in a finite 3D acoustic crystal are all based on the solution in Eq. (5). For details about the numerical method based on the finite-element analysis, please refer to Appendix A.

A. Acoustic 3D Chern insulator with a Chern vector $\boldsymbol{C} = (0, 0, 1)$

We start with the celebrated 2D Haldane model [1] and its acoustic realization, the acoustic 2D Chern insulator, as shown in Fig. 6(a). The hexagonal prisms with three attached pillars represent the sublattice sites, whose on-site potentials can be tuned by changing the side widths of the pillars denoted as R_A and R_B [Fig. 6(a)]. The on-site potential difference $\Delta R = (R_A - R_B)/2$ represents the inversion symmetry (IS)-breaking strength. In addition, the sites within each sublattice (Sites A or Sites B) are coupled by a circulating airflow (small red and blue arrows) to implement the complex next-nearest-neighboring hopping, and the circumferential speed v of the flow characterizes the TRS breaking strength [17–20,32]. The two sublattices are slightly shifted vertically to avoid self-intersecting, and the real nearest-neighboring hopping between neighboring sites are implemented by Z-shaped air tubes. Note that such TRS breaking by airflow has been utilized to realize an acoustic 2D Chern insulator [20].

By stacking the acoustic 2D Haldane model periodically along the vertical direction with vertical and chiral interlayer couplings, we can construct an acoustic realization of the 3D Haldane model with the effective magnetic field $\boldsymbol{B}_{\rm eff}$ parallel to the z axis, as shown in Figs. 6(b) and 6(c). The vertical (t_a, t_b) and chiral (t_c) interlayer couplings are controlled by the side widths of the corresponding air tubes denoted as r_a, r_b, and r_c, as shown in Fig. 6(b). The chiral hopping is introduced to guarantee the emergence of ideal type-I Weyl points, facilitating the opening of a 3D complete bandgap with a relatively small TRS-breaking strength. When varying the TRS (v) and IS (ΔR) breaking strengths, the calculated phase diagram of the acoustic 3D Haldane model exhibits

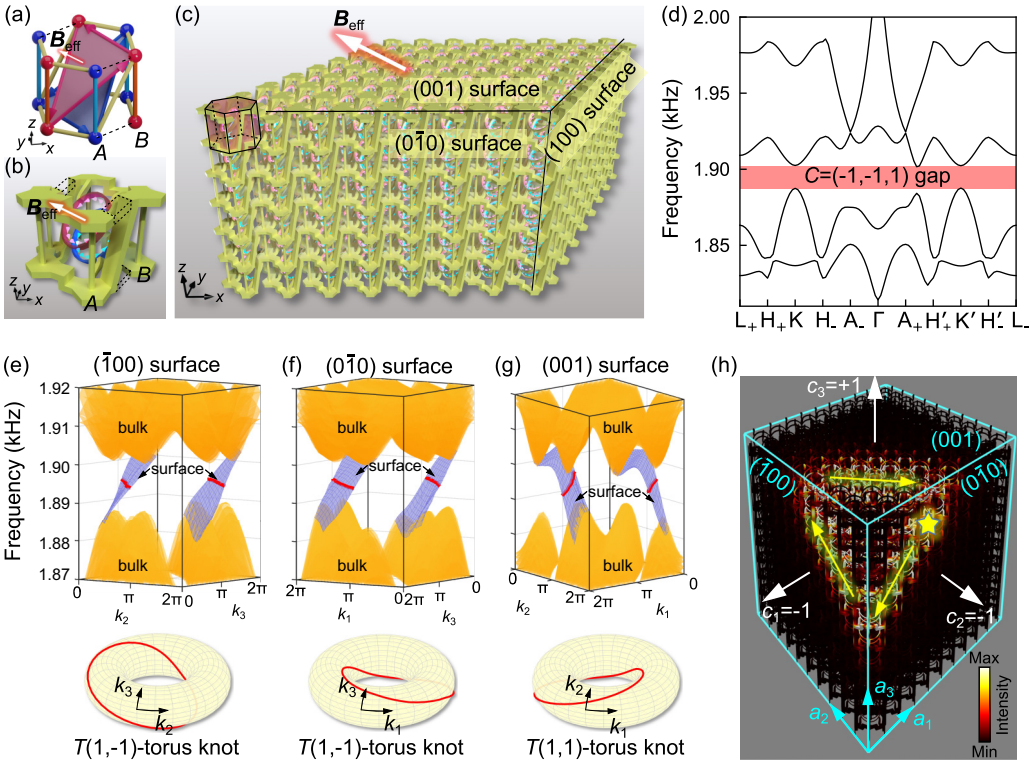

FIG. 7. Acoustic 3D Chern insulator with a Chern vector $\boldsymbol{C} = (-1, -1, 1)$. (a) The tilted 3D Haldane model and (b) its acoustic realization, in which the circulating airflows (blue and red arrows) are tilted to induce nonreciprocal hoppings between adjacent layers. (c) Schematic view of the acoustic 3D Chern insulator with a Chern vector $\boldsymbol{C} = (-1, -1, 1)$. (d) The simulated bulk band structure of the acoustic 3D Chern insulator with a 3D topological $\boldsymbol{C} = (-1, -1, 1)$ band gap. (e)–(g) The chiral surface states dispersions (blue sheets) of the left ($\bar{1}$00), front (0$\bar{1}$0), and top (001) surfaces, respectively. The bottom panels show the torus knots formed by winding the Fermi loops on three different surface BZs. (h) Full-wave simulated acoustic intensity distributions of the chiral surface states excited by a point source (yellow star) at 1.897 kHz on the surfaces of an acoustic 3D Chern insulator with a Chern vector $\boldsymbol{C} = (-1, -1, 1)$.

three different topological phases, including trivial insulators, Weyl semimetals, and 3D Chern insulators. Figure 6(d) shows the bulk band structure of an acoustic 3D Chern insulator with $\Delta R = 0$ and $v = 6$ m/s, which opens a 3D topological bandgap with a nontrivial Chern vector $\boldsymbol{C} = (0, 0, 1)$. To gain more insights into the topological surface states of the acoustic 3D Chern insulator, Fig. 6(e) presents the front (0$\bar{1}$0) surface dispersion of the acoustic 3D Chern insulator (blue sheet), in which the red curve represents the Fermi loop. It can be seen that the chiral surface states always exist for any k_3 and span the whole bandgap with negative group velocity. Since the Chern vector has only a single nonzero Chern number c_3, the Fermi loop winds a cycle only along k_3 direction but not k_1 direction, forming a simple loop (i.e., the unknot) on the 2D surface Brillouin zone (BZ). We then perform full-wave simulations to demonstrate the one-way and robust transport of the acoustic chiral surface states. As shown in Fig. 6(f), a point source (yellow star) is placed at the center of (0$\bar{1}$0) surface. The excited acoustic chiral surface states propagate nonreciprocally and route around two sharp corners without notable reflection. Even if we insert a solid defect in the path of the chiral surface states, or we introduce randomly distributed on-site potentials as long as the Chern bandgap is not close, they still can bypass the obstacle with negligible reflection, revealing the topological protection of the acoustic chiral surface states (see Appendix B for comparison).

B. Acoustic 3D Chern insulator with a Chern vector $\boldsymbol{C} = (-1, -1, 1)$

Next, we demonstrate that, by tilting the circulating airflows and the effective magnetic fields, we can construct an acoustic 3D Chern insulator with a Chern vector $\boldsymbol{C} = (-1, -1, 1)$ that supports chiral surface states on all six surfaces, instead of only the four side surfaces. These chiral surface states can form reflectionless topological negative refraction at the one-dimensional hinges separating different facets. As shown in Figs. 7(a)–7(c), all circulating airflows (small blue and red arrows) are tilted and each of them couples three sublattice sites residing in adjacent layers in order to keep consistent with the tight-binding configuration of the tilted 3D Haldane model shown in Fig. 5(a). Consequently, the effective magnetic field $\boldsymbol{B}_{\text{eff}}$ is tilted with nonzero components along all primitive lattice vectors $\boldsymbol{a}_i$. Meanwhile, four NN hoppings (black dashed lines) are replaced by two slanted interlayer couplings (tilted yellow tubes) between different sublattice sites, tilting the 3D honeycomb lattice in accordance with the tilted effective magnetic fields $\boldsymbol{B}_{\text{eff}}$. Such a tilted 3D Haldane model can be approximately described by a new Hamiltonian modified from the previously discussed 3D Haldane model, and the Wilson-loop calculation of the tilted 3D Haldane model exhibits a 3D Chern insulating phase with a Chern vector $\boldsymbol{C} = (-1, -1, 1)$, as we have already

described in Sec. II B. Figure 7(d) shows the simulated bulk band structure of the acoustic 3D Chern insulator, which exhibits a complete nontrivial topological Chern band gap with a Chern vector $\boldsymbol{C} = (-1,\ -1,\ 1)$.

Compared with the acoustic 3D Chern insulator with a Chern vector $\boldsymbol{C} = (0,\ 0,\ 1)$, the acoustic 3D Chern insulator with a Chern vector $\boldsymbol{C} = (-1,\ -1,\ 1)$ exhibits two unique features. First, the latter supports chiral surface states on all surfaces, as shown in Figs. 7(e)–7(g). Second, for the latter, the Fermi loops wind around both the median and longitude of the surface BZ torus (the 2D surface BZs formed by two k_i), as shown in the bottom panels of Figs. 7(e)–7(g). Moreover, the winding numbers and winding directions of the Fermi loops can be fully determined by the Chern vector. Take the $(\bar{1}00)$ surface as an example, the Chern vector components $c_2 = -1$ and $c_3 = 1$ imply that the Fermi loop wraps along both k_2 and k_3 axes for one cycle but with opposite directions, forming a $T(-1,\ 1)$ [or equivalently, $T(1,\ -1)$] torus knot. Similarly, $c_1 = -1$ and $c_3 = 1$ leads to a $T(1,\ -1)$ torus knot on the $(0\bar{1}0)$ surface, and $c_1 = -1$ and $c_2 = -1$ results in a $T(1,\ 1)$ torus knot on the (001) surface, as shown in the bottom panels of Figs. 7(e)–7(g), respectively.

Now we study the propagation of chiral surface states on the acoustic 3D Chern insulator with a Chern vector $\boldsymbol{C} = (-1,\ -1,\ 1)$, as shown in Fig. 7(h). A point source (yellow star) is placed on the $(0\bar{1}0)$ surface to excite the chiral surface states. It can be seen that the chiral surface states propagate unidirectionally (yellow arrows) on three different adjacent surfaces. More interestingly, we find that nonreciprocal and reflectionless topological negative refraction of chiral surface states occurs at the edges between any two adjacent surfaces, which can be explained by the isofrequency contour analysis on two adjacent surfaces. In fact, the direction of group velocity $\boldsymbol{v}_g$ of the chiral surface states can be identified approximately as in the direction of $\boldsymbol{n} \times \boldsymbol{C}$, where $\boldsymbol{n}$ is the normal vector of the surface. A graphical illustration of this rule is provided in Appendix C, which predicts the propagation and refraction direction of the chiral surface states, matching well with the simulated results in Fig. 7(h). It also shows that for an arbitrary surface of a 3D Chern insulator, the chiral surface states can exist as long as the Chern vector $\boldsymbol{C}$ is not in parallel with the normal vector $\boldsymbol{n}$.

C. Discussion on the arbitrary Chern vectors

Finally, we demonstrate that 3D Chern insulating phases with arbitrary Chern vectors $\boldsymbol{C} = (-N_1,\ -N_2, N_3)$ can be constructed by adopting a supercell comprising $N_1 \times N_2 \times N_3$ elementary tilted unit cells shown in Fig. 8(a). For instance, Fig. 8(a) shows a 3D tight-binding model of a supercell consisting of $2 \times 3 \times 6$ elementary tilted unit cells, representing a 3D Chern insulating phase with a Chern vector $\boldsymbol{C} = (-2,\ -3,\ 6)$. The inter- and intrasupercell hopping strengths are staggered to ensure the selected supercell to be the irreducible primitive unit cell. Due to limited computational resources, we only perform calculation of the multifold supercell based on its tight-binding Hamiltonian instead of full-wave simulation. The calculated surface DOS of $(\bar{1}00)$, $(0\bar{1}0)$, and (001) surfaces in Figs. 8(b)–8(d) reveal multiple chiral surface states on different surfaces due to the large

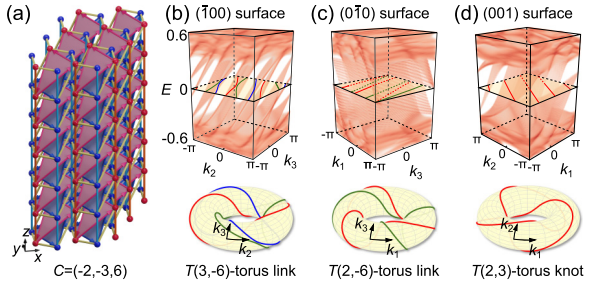

FIG. 8. 3D Chern insulating phases with arbitrary Chern vectors $\boldsymbol{C} = (-N_1,\ -N_2, N_3)$. (a) The tight-binding configuration of a $2 \times 3 \times 6$ supercell with a Chern vector $\boldsymbol{C} = (-2,\ -3,\ 6)$. (b)–(d) Calculated surface dispersions (top panel) and zero-energy surface DOS (bottom panel) on the $(\bar{1}00)$, $(0\bar{1}0)$, and (001) surfaces of the 3D Chern insulator shown in (a). The zero-energy Fermi loops (red, green, and blue curved lines) in (b)–(d) form distinct torus knots or torus links on different surface BZ whose characteristic integers are determined by the Chern vector. The tight-binding parameters are $t_1 = 1, t_2 = -0.2, t_a = -t_b = 0.2, M = 0, \phi = 0.5\pi$.

Chern numbers. Moreover, we find that the winding behaviors of the Fermi loops, namely, the torus knots or links formed on the 2D surface BZs, can be greatly enriched in 3D Chern insulating phases with arbitrary Chern vectors. As shown in Fig. 8(b), the Fermi loops on the $(\bar{1}00)$ surface form a $T(-3,\ 6)$ torus link because $c_2 = -3$ and $c_3 = 6$. Since 3 and 6 are not coprime, the Fermi loops are three interlinked $T(-1,\ 2)$ [or equivalently, $T(1,\ -2)$] torus knots (red, green, and blue twisted loops) according to the knot theory [33]. Each of the three torus knots winds one cycle along k_2 axis and two cycles along k_3 axis in the opposite direction. Similarly, the Fermi loop on the $(0\bar{1}0)$ surface forms a $T(2,\ -6)$ torus link [or equivalently, two interlinked $T(1,\ -3)$ torus knots (red and green twisted loops)] as shown in Fig. 8(c). The situation is different for the (001) surface, since, as shown in Fig. 8(d), the Fermi loop forms a single $T(2,\ 3)$ torus knot (red twisted loop) because $c_1 = -2$ and $c_2 = -3$. Note that these torus knots or torus links are formed in a single 3D Chern insulator, in contrast to the previously reported torus links or Hopf links formed at an interface between two different 3D Chern insulators with perpendicular Chern vectors [14].

Besides the above scheme to construct 3D Chern insulating phases with arbitrary Chern vectors, there are two other approaches to achieve this goal. The first one is modifying the nonreciprocal couplings in adjacent layers. In the current design, the nonreciprocal couplings are arranged between the nth layer and the $(n + \Delta n)$th layer with $\Delta n = 1$. If we increase Δn, we can achieve arbitrary Chern vectors with components proportional to Δn. The second way is to add long-range intralayer couplings, which have been used to realize large Chern numbers in 2D Chern insulators. In Appendix D, we show two examples of these two schemes to achieve arbitrary Chern vectors.

IV. CONCLUSIONS

In conclusion, we have extended the 3D Chern insulator phase to acoustic crystals and proposed a scheme to construct

arbitrary Chern vectors with multiple nonzero components. The arbitrary Chern vector allows the existence of chiral surface states on all six surfaces and the emergence of surface-state torus knots or links on the surface of a single 3D Chern insulator, unlike the previous realization of photonic 3D Chern insulators that only support chiral surface states on four side surfaces parallel to the Chern vector and require an internal domain wall between two crystals with perpendicular Chern vectors for such phenomena. Moreover, when the chiral surface states propagate around two adjacent surfaces, a novel phenomenon termed chiral topological negative refraction occurs, which is different from the previous reported topological negative refractions [30,31] due to the TRS breaking. Our work thus provides a full picture of the bulk-boundary correspondence for the topological Chern vector. Since the acoustic 2D Chern insulator has recently been successfully realized [20], we envision that a similar implementation in 3D should be feasible in the near future.

ACKNOWLEDGMENTS

This work was supported by the National Natural Science Foundation of China (62375118, 62361166627, 12104211, 62220106006, 12304484, 62175215, 11961141010, 61975176, 12404053, 62405053, and 92265201), the Guangdong Basic and Applied Basic Research Foundation (2024A1515012770, 2024A1515011371, 2025A1515012284, and 2025A1515012229), the Shenzhen Science and Technology Program (20220815111105001 and 202308073000209), High level of special funds under Grant No. G03034K004, China Postdoctoral Science Foundation (2023M731533), National Research Foundation Singapore Competitive Research Program (NRF-CRP23-2019-000), Singapore Ministry of Education Academic Research Fund Tier 2 (MOE2019-T2-2-085), the Key Research and Development Program of the Ministry of Science and Technology (2022YFA1405200, 2022YFA1404900, 2022YFA1404704, and 2022YFA1404902), the Fundamental Research Funds for the Central Universities (2021FZZX001-19), the Key Research and Development Program of Zhejiang Province (2022C01036), the Excellent Young Scientists Fund Program (Overseas) of China, Research Center for Industries of the Future (RCIF) at Westlake University (210000006022312), Westlake Education Foundation (103110736022301), and the Innovation Program for Quantum Science and Technology (Grant No. 2021ZD0302704).

DATA AVAILABILITY

The data that support the findings of this article are not publicly available upon publication because it is not technically feasible and/or the cost of preparing, depositing, and hosting the data would be prohibitive within the terms of this research project. The data are available from the authors upon reasonable request.

APPENDIX A: SIMULATION METHOD OF THE ACOUSTIC CHERN INSULATOR

1. Acoustic bulk and surface band structure calculations

When considering the acoustic wave function $\psi(\boldsymbol{r})$ propagating in the periodic acoustic crystal, its Bloch wave form gives $\psi_{n\mathrm{k}}(\boldsymbol{r}) = u_{n\mathrm{k}}(\boldsymbol{r})\exp(i\boldsymbol{k}\cdot\boldsymbol{r})$, where $\boldsymbol{k}$ labels the wave vector in the first BZ, and the cell-periodic functions $u_{n\mathrm{k}}(\boldsymbol{r})$ is translational invariant under any primitive lattice vectors. With such a denotation, Eq. (5) could be further transformed to the following form:

$$[\nabla + i(\boldsymbol{k} - \boldsymbol{A})]\cdot[\nabla + i(\boldsymbol{k} - \boldsymbol{A})]u_{n\mathrm{k}} + \frac{\omega^2}{c_0^2}u_{n\mathrm{k}} = 0. \quad \text{(A1)}$$

For each given wave vector $\boldsymbol{k}$, Eq. (A1) can be regarded as an eigenproblem with ω and $u_{n\mathrm{k}}$ the eigenfrequency and eigenfunction, respectively. It can be readily solved by using the partial differential equation (PDE) interface of the mathematical module of COMSOL MULTIPHYSICS, in which the general form of a second-order PDE is

$$\lambda^2 e_a u - \lambda d_a u + \nabla\cdot(-c\nabla u - \alpha u + \gamma) + \beta\cdot\nabla u + au = f. \quad \text{(A2)}$$

So, we can obtain the dispersion relation $\omega = \omega(\mathrm{k})$ by using the eigenvalue solver of COMSOL with the eigenvalue denoted as $\lambda = i\omega$, and the other coefficients $\mathrm{e_a} = 1/c_0^2$, $\mathrm{c} = 1$, $\alpha = i(\boldsymbol{k} - \boldsymbol{A})$, $\beta = -i(\boldsymbol{k} - \boldsymbol{A})$, $\gamma = 0$, $\mathrm{a} = |\boldsymbol{k} - \boldsymbol{A}|^2$. Note that periodic conditions at the unit cell boundaries should be applied on the unknown variable $\mathrm{u} \equiv u_{n\mathrm{k}}$. In the simulation, the background medium (air) is modeled with a mass density of $1.2\,\mathrm{kg\,m^{-3}}$ and a sound speed of $346\,\mathrm{m\,s^{-1}}$. The surrounding solid material can be considered as hard boundaries due to the substantial acoustic impedance contrast compared with air.

2. Finite-size sample calculations

When considering the acoustic wave propagation in the presence of an external harmonic source $f(\boldsymbol{r}_0) = F_0\delta(\boldsymbol{r}_0)\exp(-i\omega t)$ located at $\boldsymbol{r}_0$, where F_0 denotes the amplitude of the excitation force and $\delta(\boldsymbol{r})$ denotes the Dirac delta function, the wave equation Eq. (4) with an additional source term reads

$$(\nabla - i\boldsymbol{A})\cdot(\nabla - i\boldsymbol{A})\psi(\boldsymbol{r}) + \frac{\omega^2}{c_0^2}\psi(\boldsymbol{r}) = F_0\delta(\boldsymbol{r} - \boldsymbol{r}_0). \quad \text{(A3)}$$

In this case, the excitation frequency ω is predesignated, and solving the above equation in terms of $\psi(\mathrm{r})$ actually turns into a static problem. To do so, we use the stationary study type of the general PDE interface of COMSOL, whose general form is

$$e_a\frac{\partial^2 u}{\partial t^2} + d_a\frac{\partial u}{\partial t} + \nabla\cdot(-c\nabla u - \alpha u + \gamma) + \beta\cdot\nabla u + au = f \quad \text{(A4)}$$

in which the parameter set-ups are $e_a = d_a = 0$, $c = 1$, $\alpha = -i\boldsymbol{A}$, $\beta = i\boldsymbol{A}$, $\gamma = 0$, $a = |\boldsymbol{A}|^2 - \omega^2/c_0^2$.

APPENDIX B: ROBUSTNESS OF THE CHIRAL SURFACE STATES

In this section, we perform full-wave simulations to probe the chiral and robust propagation of the 3D Chern insulator's surface states, by taking the 3D acoustic Chern insulator with a Chern vector $\boldsymbol{C} = (0,\ 0,\ 1)$ as an example. We demonstrate the robustness of the chiral surface states by considering the existence of defects and disorder, respectively.

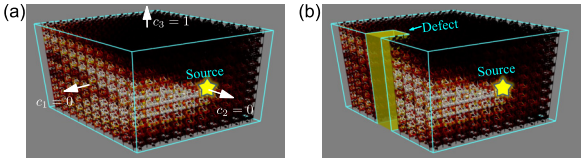

FIG. 9. Robustness of the chiral surface states against defects. The simulated acoustic pressure distribution of the chiral surface state under a monopole source excitation near the center of the right surface of an acoustic 3D Chern insulator. (a) A perfect 3D acoustic Chern insulator with $10 \times 10 \times 10$ unit cells. (b) A 3D acoustic Chern insulator with a defect introduced by removing $2 \times 2 \times 10$ cells.

Robustness against defects. We first built a 3D acoustic crystal with the fundamental building blocks being the unit cell shown in Fig. 6(b) in the main text. The 3D acoustic crystal consists of $10 \times 10 \times 10$ unit cells, as shown in Fig. 9(a). To excite the surface states in the finite-element simulation, we put a monopole source near the center of the right surface (yellow star). The computed acoustic wave field (the sound pressure distribution) is shown in Fig. 9(a), which clearly shows the surface states propagating clockwise around the z axis, indicating its chirality. Next, we introduce a line defect in the perfect crystal by removing $2 \times 2 \times 10$ cells, as shown in Fig. 9(b). We set the same source excitation as that in Fig. 9(a), and observe that the chiral surface states can bypass the defect without any backscattering or reflections, demonstrating that the chiral surface state of a 3D Chern insulator is robust against structural defects.

Robustness against disorder. It is a rather difficult and even an unreachable task to build a full 3D disordered acoustic Chern insulator. Since we have shown that 3D acoustic Chern insulators can be qualitatively and accurately described by the tight-binding model (TBM), here we alternatively choose to construct a 3D crystal based on the TBM and investigate the robustness of chiral surface state transmission when random on-site potentials are introduced.

The schematic of the 3D crystal composed of $12 \times 12 \times 12$ unit cells is shown in Fig. 10(a), where the yellow star denotes the location of a point source, and the yellow arrows represent the propagation direction of the chiral surface state. We introduce a randomly distributed potential ranging from $[-\delta M, \delta M]$ on all the sites independently, including those both on the surface and in the bulk. In our case, the chiral surface states propagate in the clockwise direction when $\delta M = 0$. To characterize this unidirectionality, we first collect the wave intensities along two lines ($l_{1,2}$) that are equally spaced on both sides of the source, which we denote as $T_{1,2}$, and we introduce a factor η defined as

$$\eta = \frac{T_1 - T_2}{T_1 + T_2}. \tag{B1}$$

It is evident that a pure clockwise or counterclockwise chiral surface state corresponds $\eta = 1$ or $\eta = -1$, respectively. Any median value of η indicates that the surface state propagates along both directions. We note that $T_{1,2} = T_{1,2}(\delta M)$ is the total wave intensities of all the sites located on the line $l_{1,2}$,

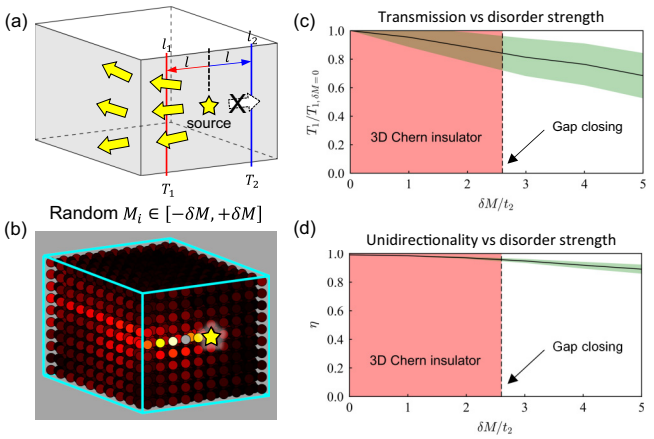

FIG. 10. Robustness of the chiral surface states of 3D Chern insulator against the on-site potential disorder. (a) Schematic of the 3D Chern insulator and its chiral surface states. (b) The energy distribution of the chiral surface states under a point source excitation at a maximum disorder strength $\delta M = 2$ for all sites. (c) The transmission (measured by integrating the wave intensity along line l_1) ratio between disordered and ordered systems against on-site potential disorder strength. (d) The unidirectionality of the chiral surface state transmission against the on-site potential disorder strength. In (c) and (d), the results are averaged from 500 times of repeated calculations for each disorder level.

which means

$$T_{1,2}(\delta M) = \sum_{i \in l_{1,2}} |\psi_i|^2. \tag{B2}$$

Figure 10(b) shows the energy distribution under a point source excitation at a maximum disorder strength $\delta M = 2$, which maintains a good unidirectionality. Figures 10(c) and 10(d) shows how the increasement of δM impacts the transmission $T_1(\delta M)/T_1(0)$ and directional factor η. For each value of δM, we generate 500 realizations of random disordered 3D crystals, and calculate the average value and the standard deviations, as represented by the black solid lines and green shaded areas. The result in Fig. 10(c) shows that random on-site potentials can slightly decrease the transmission $T_1(\delta M)/T_1(0)$, but it can still remain a relatively high value of 85% even at the critical point when the gap is closed. While Fig. 10(d) shows that the unidirectionality is even more robust since η maintains larger than 97% before gap closing.

APPENDIX C: RELATIONSHIP BETWEEN THE GROUP VELOCITY OF THE CHIRAL SURFACE STATE AND THE CHERN VECTOR

The group velocity v_g of the chiral surface state at a specific surface can be determined by the Chern vector $\boldsymbol{C}$ and the surface normal vector $\boldsymbol{n}$ as $\boldsymbol{n} \times \boldsymbol{C}$. Take the $\boldsymbol{C} = (-1, -1, 1)$ as an example, we can first decompose it into $\boldsymbol{C} = (-1, 0, 0) + (0, -1, 0) + (0, 0, 1)$, each of which possess only one single nonzero component. This helps us to understand this rule more clearly. As shown in Fig. 11(a), the Chern vector $(-1, 0, 0)$ enforces the chiral surface states propagating along the yellow arrow, since the surface normal vector (red), the Chern vector (blue), and the group velocity

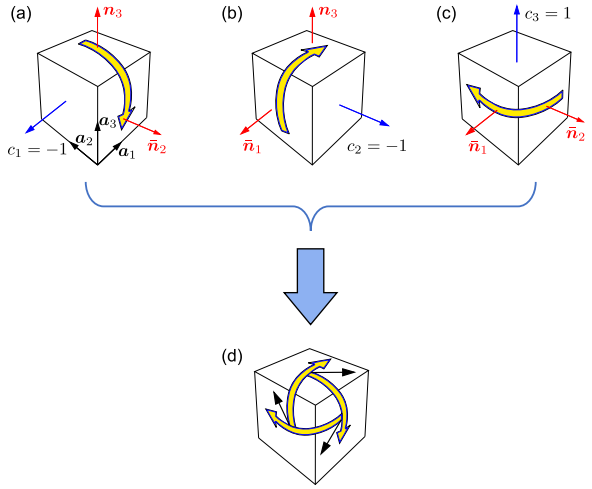

FIG. 11. The illustrations of the relationship between the group velocity of the chiral surface states and the Chern vector.

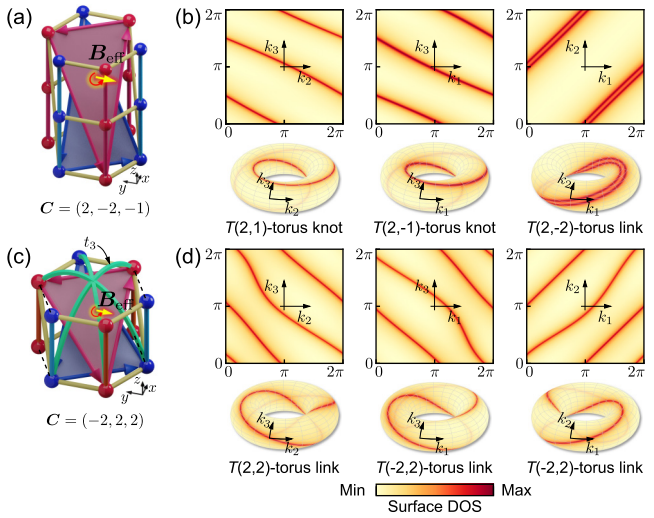

FIG. 12. The alternative ways to achieve large Chern components. (a) Non-reciprocal hoppings arranged between the nth layer and the $(n + \Delta n)$th layer with $\Delta n = 2$, which results in a Chern vector $\boldsymbol{C} = (2, -2, -1)$, as shown in (b). (c) The introduction of long-range hoppings t_3, which results in a Chern vector $\boldsymbol{C} = (-2, 2, 2)$, as shown in (d).

(yellow) conform to the right-hand rule. Similar arguments can be applied to the two decomposed Chern vectors, as shown in Figs. 11(b) and 10(c). Lastly, the superposition of the three resultant group velocities (yellow arrows) gives the final propagating directions of the chiral surface states [Fig. 11(d)], as confirmed by the simulation results in Fig. 7(h) in the main text.

APPENDIX D: TWO ALTERNATIVE WAYS TO ACHIEVE ARBITRARY CHERN VECTORS

In this section, we provide two alternative ways to achieve arbitrary Chern vectors, instead of using the way we discussed in the main text. As we have discussed in the main text, the first one is to modify the nonreciprocal couplings in adjacent layers with $\Delta n > 1$, and the second one is to add long-range intralayer hoppings. Figure 12 displays two examples of the tight-binding configurations and their corresponding surface Fermi loops. Figs. 11(a) and 12(c) display the tight-binding configurations of $\Delta n = 2$ and the case when the third-nearest-neighbor hopping t_3 are included, respectively. The Wilson loop calculations show that the Chern vectors are $\boldsymbol{C} = (2, -2, -1)$ and $\boldsymbol{C} = (-2, 2, 2)$. Their corresponding Fermi loops on different surface BZs are shown in Figs. 12(b) and 12(d), respectively.

[1] F. D. M. Haldane, Model for a quantum Hall effect without Landau levels: Condensed-matter realization of the "parity anomaly", Phys. Rev. Lett. **61**, 2015 (1988).

[2] C.-Z. Chang *et al.*, Experimental observation of the quantum anomalous Hall effect in a magnetic topological insulator, Science **340**, 167 (2013).

[3] Y. Deng, Y. Yu, M. Z. Shi, Z. Guo, Z. Xu, J. Wang, X. H. Chen, and Y. Zhang, Quantum anomalous Hall effect in intrinsic magnetic topological insulator $MnBi_2Te_4$, Science **367**, 895 (2020).

[4] Y.-F. Zhao *et al.*, Tuning the Chern number in quantum anomalous Hall insulators, Nature (London) **588**, 419 (2020).

[5] M. Serlin, C. L. Tschirhart, H. Polshyn, Y. Zhang, J. Zhu, K. Watanabe, T. Taniguchi, L. Balents, and A. F. Young, Intrinsic quantized anomalous Hall effect in a moiré heterostructure, Science **367**, 900 (2020).

[6] F. D. M. Haldane and S. Raghu, Possible realization of directional optical waveguides in photonic crystals with broken time-reversal symmetry, Phys. Rev. Lett. **100**, 013904 (2008).

[7] Z. Wang, Y. D. Chong, J. D. Joannopoulos, and M. Soljačić, Reflection-free one-way edge modes in a gyromagnetic photonic crystal, Phys. Rev. Lett. **100**, 013905 (2008).

[8] Z. Wang, Y. Chong, J. D. Joannopoulos, and M. Soljačić, Observation of unidirectional backscattering-immune topological electromagnetic states, Nature (London) **461**, 772 (2009).

[9] Y. Poo, R. Wu, Z. Lin, Y. Yang, and C. T. Chan, Experimental Realization of self-guiding unidirectional electromagnetic edge states, Phys. Rev. Lett. **106**, 093903 (2011).

[10] S. A. Skirlo, L. Lu, and M. Soljačić, Multimode one-way waveguides of large Chern numbers, Phys. Rev. Lett. **113**, 113904 (2014).

[11] S. A. Skirlo, L. Lu, Y. Igarashi, Q. Yan, J. Joannopoulos, and M. Soljačić, Experimental observation of large Chern numbers in photonic crystals, Phys. Rev. Lett. **115**, 253901 (2015).

[12] F. D. M. Haldane, Berry curvature on the Fermi surface: Anomalous Hall effect as a topological Fermi-liquid property, Phys. Rev. Lett. **93**, 206602 (2004).

[13] D. Vanderbilt, *Berry Phases in Electronic Structure Theory: Electric Polarization, Orbital Magnetization and Topological Insulators* (Cambridge University Press, Cambridge, 2018).

[14] G.-G. Liu *et al.*, Topological Chern vectors in three-dimensional photonic crystals, Nature (London) **609**, 925 (2022).

[15] C. Devescovi, M. García-Díez, I. Robredo, M. Blanco de Paz, J. Lasa-Alonso, B. Bradlyn, J. L. Mañes, M. G. Vergniory, and

A. García-Etxarri, Cubic 3D Chern photonic insulators with orientable large Chern vectors, Nat. Commun. **12**, 7330 (2021).
[16] C. Devescovi, M. García-Díez, B. Bradlyn, J. L. Mañes, M. G. Vergniory, and A. García-Etxarri, Vectorial bulk-boundary correspondence for 3D photonic Chern insulators, Adv. Opt. Mater. **10**, 2200475 (2022).
[17] Z. Yang, F. Gao, X. Shi, X. Lin, Z. Gao, Y. Chong, and B. Zhang, Topological acoustics, Phys. Rev. Lett. **114**, 114301 (2015).
[18] A. B. Khanikaev, R. Fleury, S. H. Mousavi, and A. Alu, Topologically robust sound propagation in an angular-momentum-biased graphene-like resonator lattice, Nat. Commun. **6**, 1 (2015).
[19] X. Ni, C. He, X.-C. Sun, X. Liu, M.-H. Lu, L. Feng, and Y.-F. Chen, Topologically protected one-way edge mode in networks of acoustic resonators with circulating air flow, New J. Phys. **17**, 053016 (2015).
[20] Y. Ding, Y. Peng, Y. Zhu, X. Fan, J. Yang, B. Liang, X. Zhu, X. Wan, and J. Cheng, Experimental demonstration of acoustic Chern insulators, Phys. Rev. Lett. **122**, 014302 (2019).
[21] C. He, X. Ni, H. Ge, X.-C. Sun, Y.-B. Chen, M.-H. Lu, X.-P. Liu, and Y.-F. Chen, Acoustic topological insulator and robust one-way sound transport, Nat. Phys. **12**, 1124 (2016).
[22] R. Fleury, A. B. Khanikaev, and A. Alù, Floquet topological insulators for sound, Nat. Commun. **7**, 11744 (2016).
[23] J. Lu, C. Qiu, M. Ke, and Z. Liu, Valley vortex states in sonic crystals, Phys. Rev. Lett. **116**, 093901 (2016).
[24] J. Lu, C. Qiu, L. Ye, X. Fan, M. Ke, F. Zhang, and Z. Liu, Observation of topological valley transport of sound in sonic crystals, Nat. Phys. **13**, 369 (2017).
[25] X. Zhang, M. Xiao, Y. Cheng, M.-H. Lu, and J. Christensen, Topological sound, Commun. Phys. **1**, 97 (2018).
[26] G. Ma, M. Xiao, and C. T. Chan, Topological phases in acoustic and mechanical systems, Nat. Rev. Phys. **1**, 281 (2019).
[27] C. He, H.-S. Lai, B. He, S.-Y. Yu, X. Xu, M.-H. Lu, and Y.-F. Chen, Acoustic analogues of three-dimensional topological insulators, Nat. Commun. **11**, 2318 (2020).
[28] H. Xue, Y. Yang, and B. Zhang, Topological acoustics, Nat. Rev. Mater. **7**, 974 (2022).
[29] X. Zhang, F. Zangeneh-Nejad, Z.-G. Chen, M.-H. Lu, and J. Christensen, A second wave of topological phenomena in photonics and acoustics, Nature (London) **618**, 687 (2023).
[30] H. He, C. Qiu, L. Ye, X. Cai, X. Fan, M. Ke, F. Zhang, and Z. Liu, Topological negative refraction of surface acoustic waves in a Weyl phononic crystal, Nature (London) **560**, 61 (2018).
[31] Y. Yang, H. Sun, J. Xia, H. Xue, Z. Gao, Y. Ge, D. Jia, S. Yuan, Y. Chong, and B. Zhang, Topological triply degenerate point with double Fermi arcs, Nat. Phys. **15**, 645 (2019).
[32] R. Fleury, D. L. Sounas, C. F. Sieck, M. R. Haberman, and A. Alù, Sound isolation and giant linear nonreciprocity in a compact acoustic circulator, Science **343**, 516 (2014).
[33] V. Manturov, *Knot Theory*, 2nd ed. (CRC Press, Boca Raton, 2018).